Can Surface Water Color Accurately Determine Sediment Concentration and Grain Size? A Hyperspectral Imaging Study

David Bazzett[1], Ruo-Qian Wang[2]

1 Rutgers, The State University of New Jersey, db1142@soe.rutgers.edu

2 Rutgers, The State University of New Jersey, rq.wang@rutgers.edu

This is a preprint submitted to EarthArXiv. The paper has been submitted to the journal Water for peer review.

water MDPI

Article

Can Surface Water Color Accurately Determine Sediment Concentration and Grain Size? A Hyperspectral Imaging Study

David Bazzett[1], Ruo-Qian Wang[2]

[1] Rutgers, The State University of New Jersey, db1142@soe.rutgers.edu
[2] Rutgers, The State University of New Jersey, rq.wang@rutgers.edu

Abstract: Water color changes are closely linked to variations in suspended sediment characteristics, motivating efforts to reliably determine sediment concentration and size through remote sensing. However, current turbidity measurement practices that rely on empirical correlations have not been rigorously tested and the past testing was limited to a small range of particle conditions, constraining its applicability in the field. The advancement of hyperspectral imaging technology offers new possibilities for enhancing the analysis of water color-based sediment characterization. The study analyzes hyperspectral spectra across various wavelength bands to observe behaviors based on sediment sizes and concentrations. Results indicate the light scattering of suspended sediment solution positively correlates with concentration for low concentration but negatively correlates for high concentration, while it negatively correlates with particle size for low concentration but positively correlates for high concentration. Hyperspectral vectors were used to quantify deviations from a control, showing higher differences at greater concentrations, particularly for large particles. A diagram is developed to show the particle size and concentration correlation through the spectra. Sensitivity analyses revealed increased responsiveness to concentration changes at low concentrations and a higher sensitivity to particle size changes at both low and high concentrations. The research highlights the importance of selecting appropriate wavelength bands, with higher wavelengths proving more sensitive for higher concentrations and smaller particles. This work underscores hyperspectral imaging's potential in environmental monitoring and remote sensing, revealing the complicated physics behind water color changes due to turbidity and informing the next-generation remote sensing technology for turbidity measurements.

Keywords: hyperspectral, suspended sediment, remote sensing, water color, water quality

Citation: To be added by editorial staff during production.

Academic Editor: Firstname Lastname

Received: date
Revised: date
Accepted: date
Published: date

1. Introduction

It is well known that variations of suspended sediments can result in water color changes. Scientists have long aspired to reliably determine sediment concentration by measuring the water surface color. Achieving this capability would significantly transform monitoring and management practices across diverse aquatic environments, potentially reducing the need for labor-intensive and costly field sampling work. Such advancements could save the costs of data collection, enhance real-time monitoring efficiency, and lead to more effective environmental management strategies.

Water quality testing often employs turbidity measurement standards, such as the Nephelometric Turbidity Units (NTU) [1]. However, interpreting the resultant color variations is complicated due to the dynamic interaction between the inherent optical properties (IOPs)—including sediment particle size, composition, and concentration—and the apparent optical properties (AOPs) influenced by lighting conditions [2,3]. Moreover, there is a notable inconsistency in the reporting of turbidity data. This inconsistency may stem from the use of different accepted standards—such as USEPA Method 180.1, ISO 7027, and GLI Method 2—which are not fully aligned. These standards generate a variety of measurement units, not based directly on the optical properties of light absorption and scattering by sediment suspensions, but rather on the arbitrary definition of turbidity levels [4]. To address these discrepancies, it is suggested that all turbidimeters be calibrated using precision optical attenuators, such as neutral density filters, and involve optical physics to define the turbidity level to ensure more accurate and consistent readings.

Despite the technical challenges, water color-based sediment characteristics determination has been applied in remote sensing for years. Spectral water color data from satellites and airborne sensors has been used to estimate suspended sediment in coastal waters in coastal waters [5,6], river deltas [7], and reservoirs and lakes [8,9]. Research has employed various spectral data sources, including SeaWiFS [5], MODIS [7], and Tiangong 2 Space Lab [9]. These studies have demonstrated the potential of specific spectral bands, ranging from 400 nm to 1100 nm, to effectively model and predict total suspended solids (TSS) and sediment concentrations. For example, the 665 nm band was found useful for estimating TSS in the Irish Sea [6], while near-infrared (NIR) and combinations with green or blue bands provided effective models for river deltas in Canada [7]. Laboratory data from experimental channels have also highlighted red and NIR bands in the 600-800 nm range for estimating sediment sizes varying from clay to fine sand [3,10].

However, a couple of technical challenges prevent the advancement of this application which typically relies on field sampling for ground truth data [11,12]. First, the accuracy of the studies spans a wide range of R-square scores. This is partly due to the fact that the ground-truth data from the field is costly to collect so the validation is usually limited to specific locations and field conditions, preventing the scale-up from one location to another. Second, despite initial success in determining concentration, particle size's effect on color response was relatively less studied. It is still unclear how the sensitivity of remote sensing in discerning various sediment concentrations in addition to particle sizes [2,3]. A further study in controlled environments is required to fully examine the scaling and particle size issues.

The advancement of hyperspectral imaging technology has marked a significant leap forward in color sensing and analysis. It transcends the capabilities of conventional imaging by capturing a comprehensive, high-resolution spectrum for each image pixel, thereby unveiling subtle distinctions in material optical signatures [13]. This technology, with its origins in remote sensing applications, has proven valuable in environmental studies, both terrestrial and aquatic [14,15]. Its deployment in laboratory experiments to scrutinize suspended sediments underscores the technology's analytical potency [3,10].

This paper endeavors to test the hypothesis that the color of water rendered by hyperspectral and traditional RGB imaging can serve as a dependable indicator for sediment concentration and particle size. We examine the correlation between spectral signatures and sediment attributes through systematic lab experiments employing a hyperspectral camera. Our research aims to delineate the capabilities and constraints of hyperspectral imaging in sediment analysis. By doing so, we intend to refine the understanding of its use in environmental surveillance and aid in enhancing remote sensing methodologies.

2. Materials and Methods

Samples of sand were taken from a quarry in New Egypt, NJ. Bulk sand was passed through a 2.0 mm sieve (#10 size), and the remaining extra-large particles were discarded. Warm water was added to the remaining sediment and mixed to motivate the fine particles into suspension. This suspension of fine particles was decanted into a tray and placed in an oven. The remaining coarse particles were washed with detergent and warm water and stirred to remove the remaining attached fine particles. The wash water was dumped and refilled until it ran clear (indicating that most fine particles were removed), and these coarse particles were then placed in a separate tray and put in the oven.

The samples were left in the oven at 100°C overnight to remove moisture. The coarse sediments were then placed into a sieve array and shaken for 15 minutes in a motorized sieve shaker. The sieved sediments were then labeled and stored. These washed sediments yielded little or no sediments passing the 75 μm sieve. For the fine sediments recovered from decanting, oven-drying created plate-like pieces of mixed clay, silt, and sand that were pulverized by hand prior to sieving. Only the particles passing the 75 μm sieve were retained from the sieving of these sediments. The remaining sediments from this sample were discarded. All the sizes of the prepared sediment samples are listed in Table 1. Note that the average diameter of the sediment was obtained as the average of the upper and lower bounds of the sieve sizes.

To further refine the smallest sediments, a portion of <75 μm sediment was stirred with detergent in a 600-mL beaker and left to settle for five minutes. The liquid was decanted and discarded, and the settled sediments were recovered. This process was repeated two more times to remove the finest material, and based on the Stokes settling velocity, the estimated particle size for this sample ranges from 30-75 μm.

The sieved sediments were weighed into sample cups using an Ohaus digital scale. A 600-mL beaker containing 500 mL of cool tap water was used for this experiment. The beaker was placed on a Fisher FS Rt Basic Stirrer 120, and a magnetic stirring bead was added. This setup was on a table with a black background, with white paper included in the image. These black and white backgrounds served as control data.

Sediment was added to the beaker, and the stirrer was turned on. Sediment was added in increments, and images were captured for each increment with a Hyspex Baldur V-1024 N hyperspectral camera and the Hyspex Ground software. The camera captures 113 data channels from visible and near-infrared (VNIR), spanning 400-1000 nm wavelengths. A lens with a 3-m focal length was used, and the camera was 3 m from the mixer and beaker. At a distance of 3 m, the pixel resolution was roughly 0.9 mm x 0.9 mm. Radiometric calibration was performed on the images using Hyspex Rad software to convert the raw data to spectral radiance with units of watts * meters^{-2} * steradian^{-1}.

An overhead LED lighting was used in the experiment and a supplementary 40 W incandescent light bulb to provide IR signals in the 700-1000 nm range. Window curtains were lowered to minimize the impact of outdoor lighting. The placement of the camera and lighting sources is shown in Figure 1.

Table 1. Sediment Sizes

Size Range (μm)	Average Particle Size, d (μm)
425-850	637.5
250-425	337.5
150-250	200.0
75-150	112.5
30-75	52.5
0-75	37.5

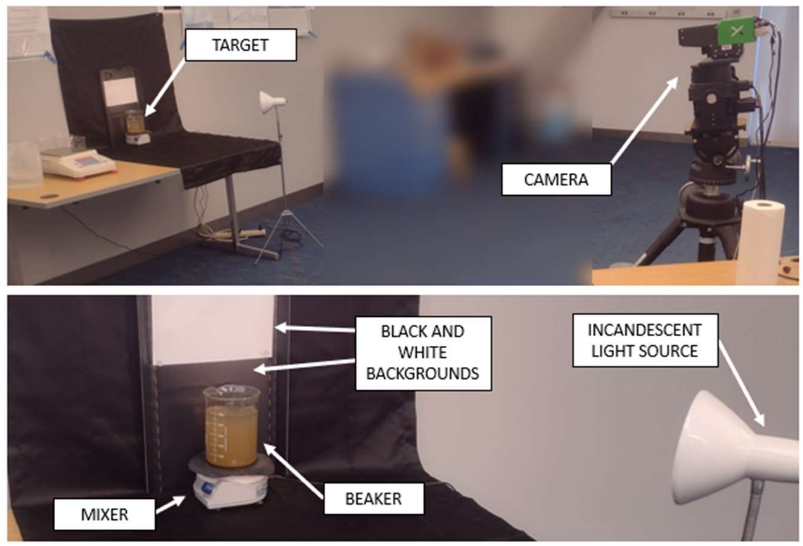

Figure 1. Experiment configuration showing the positions of the beaker, black and white background, camera, and supplemental light source.

3. Results

Three samples of pixels were taken from each image: 20x30 pixels of sediment data at the bottom of the beaker where the sediment was fully mixed, and 15x20 pixels of control data taken from both the black and white image background. For both sediment and control samples, the average and standard deviation were calculated across the horizontal and vertical dimensions, and this data was stored for each of the 113 data channels (113x30x20 data recorded per image). A sample image is shown below in Figure 2 with the experiment and control data pixels outlined in boxes. From within the sediment data, boxplots of radiance values were created for each band, as shown in Figure 3. The distribution of boxplot data shows the importance of recording the standard deviation in addition to the average radiance value.

Figure 2 shows the location of the 3 image subsets. For 113 channels, the average and standard deviation across the pixels are recorded in a table (113 x 2 = 226 recorded values). This process is repeated for the sediment, white control, and black control data, resulting in 678 recorded values per image.

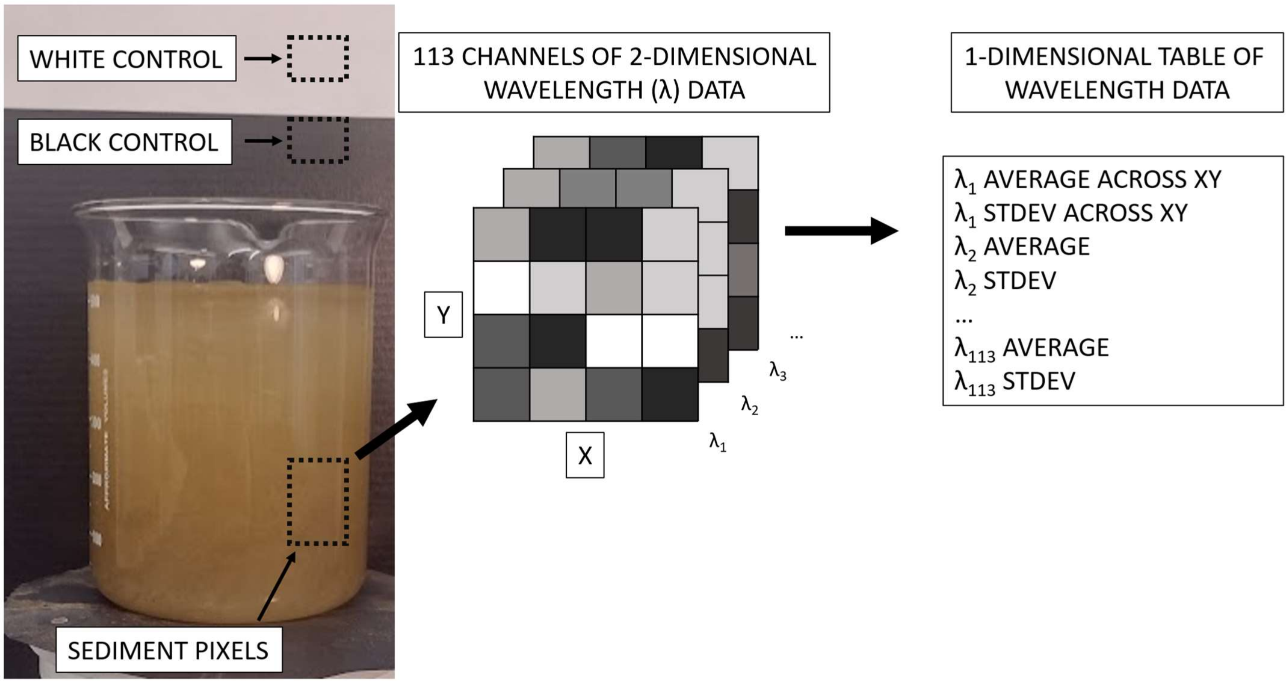

Figure 2. The location and data processing of the raw images.

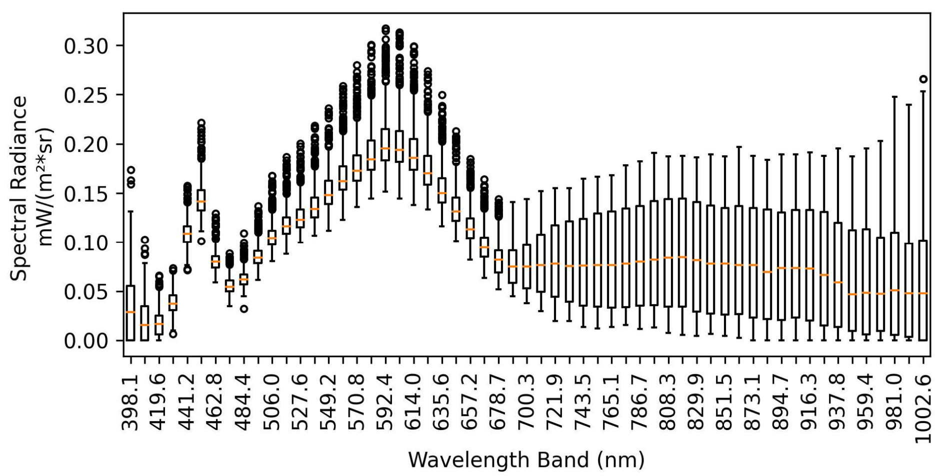

Figure 3. For the sediment pixels in a sample image, boxplots show the distribution of pixel values in the XY dimension for each channel (wavelength band) of data. Some channels have been omitted for visibility.

Analysis of the control data showed that the radiance of the background paper could vary by 1-2% for the bands between 430-1000 nm. Greater variation up to 50% was observed in the bands between 400 to 430 nm – the signal from these bands was relatively weak. Figure 3 shows the distribution of values for the sediment pixels of one example image – there is a larger spread of data for the wavelengths >700 nm.

Typical spectral curves are shown in Figure 4 for two sediment sizes. For bands between 400-680 nm, the plots of average radiance show that when more sediment is added to the water, the reflected radiance increases some amount before decreasing. Initial small concentrations increase the scattering of light, but after a threshold, the additional sediment makes the water darker and cloudier, and the signal gets weaker. This is due to both the dark color of the sediment and the sediment preventing the rays of light from penetrating the sample.

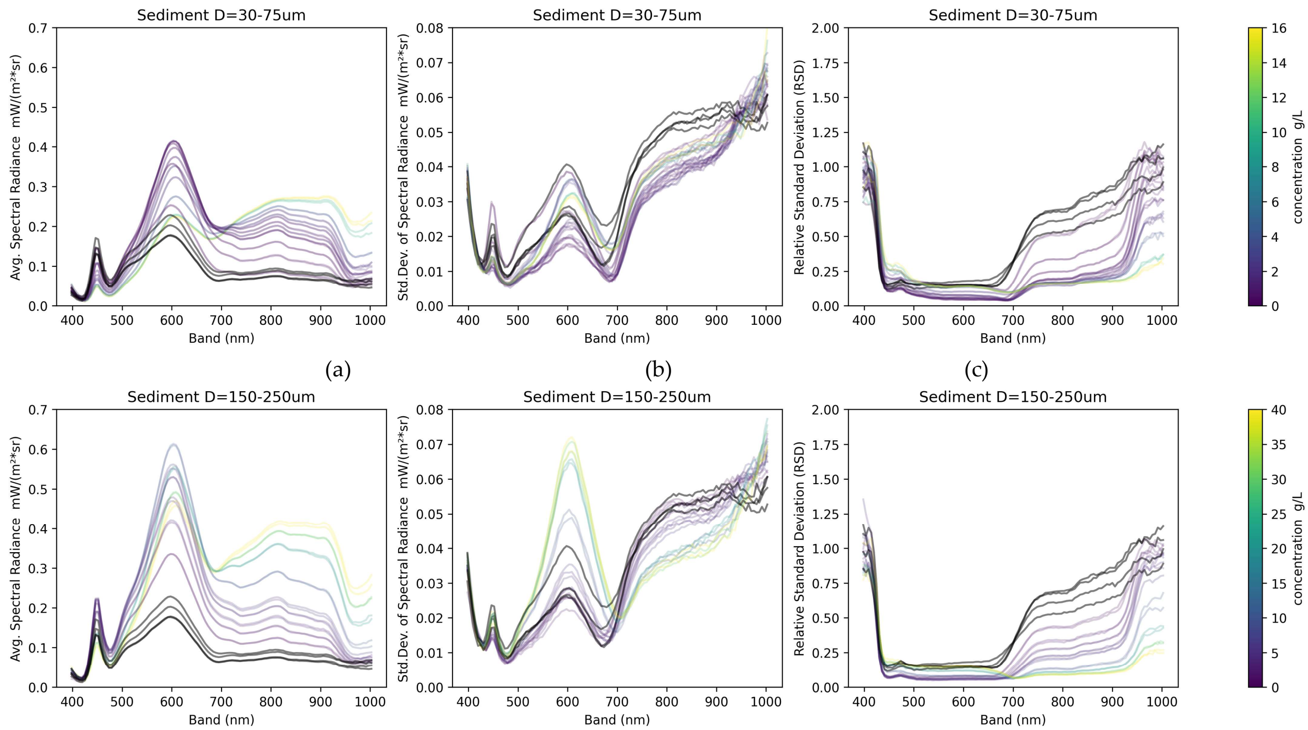

(d) (e) (f)

Figure 4. Radiance average (**a**, **d**), radiance standard deviation (**b**, **e**), and RSD values (**c**, **f**) for two different concentrations of 30-75um sediment and 150-250um sediment (top and bottom rows). Note that different ranges of concentrations were used. Baseline data with no sediment is shown in black.

For bands between 680-950 nm (roughly the Near Infrared band), the average radiance increases when more sediment is added to the water, with no inflection point or decrease recorded within the tested concentrations. This is also shown in the sensitivity analysis later.

In addition to the average radiance, the standard deviation of radiance for each wavelength band was also recorded in Figures 4b and 4e. The ratio of standard deviation over the average gives the relative standard deviation (RSD, also known as the coefficient of variation, CV), which is useful for understanding the variation in each band. The plots of RSD values show that the bands of 400-430 nm have large variations regardless of sediment size and concentration. Bands 430-680 nm (visible light) show little variation relative to the average values. Bands 680-1000 nm have higher variation at low concentrations, but the variation decreases as the sediment concentration increases. This trend can be explained by sediment scattering light in the 680-1000 nm bands, and higher concentration causes greater reflection, and the signal becomes stronger relative to the standard deviation and more homogeneous.

For each image, the average radiance signal from the white background is present in the background, so we can use this signal as a proxy for the incoming light that is shining on the beaker with sediment and calculate the sediment radiance as a percentage of the incoming light. The results are shown in Figure 5, and the trends described above are more apparent: from 400-430 nm, the percentage was extremely high because weak incident lighting was available; from 430-680 nm, the signal increased then decreased as concentration increased; and from 680-1000 nm, a higher concentration results in an increased radiance.

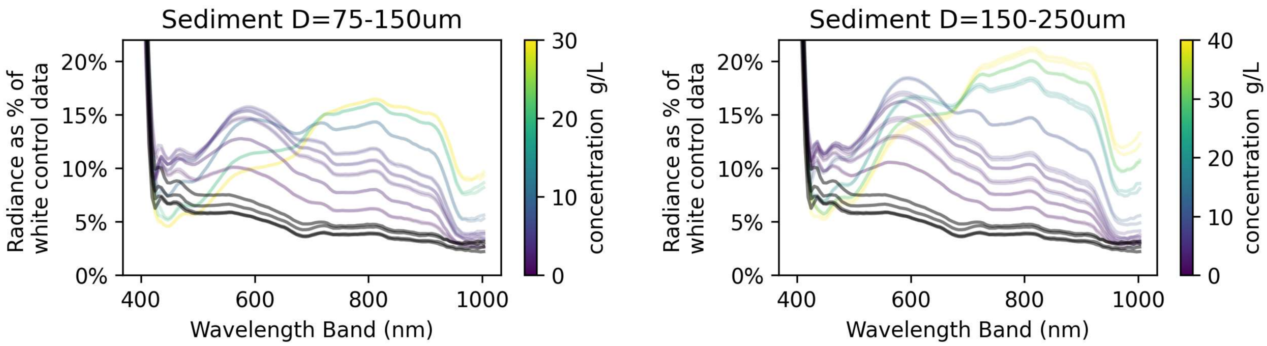

(a) (b)

Figure 5. Relative radiance of two selected particle sizes.

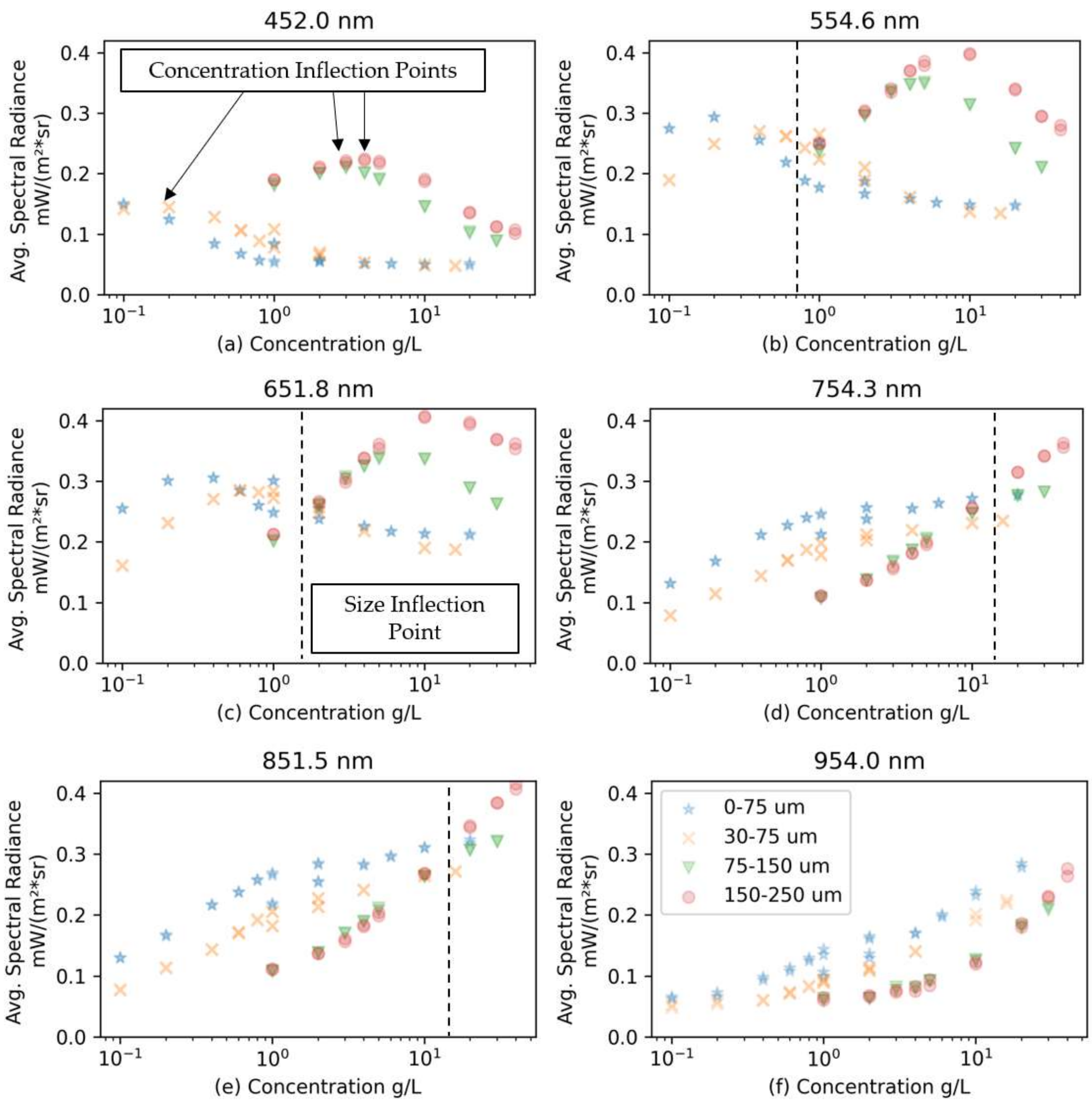

Figure 6. The radiance of the hyperspectral imaging with different concentrations and particle sizes (denoted with different symbols) for six selected spectral bands. Typical inflection points based on concentration are denoted in Figure 6a, and inflection points based on size were marked by dash lines. (Wavelengths: a- 452.0 nm, b- 554.6 nm, c- 651.8 nm, d- 754.3 nm, e- 851.5 nm, f- 954.0 nm).

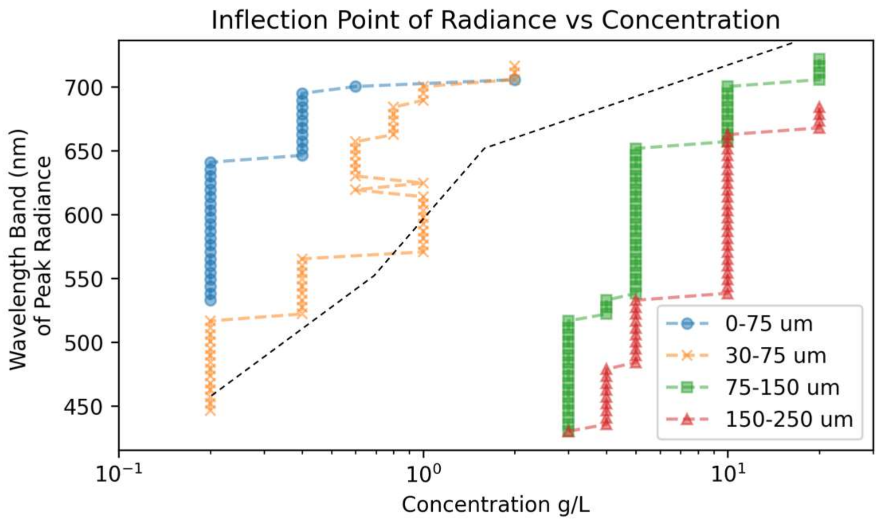

Figure 7. The inflection points for each size and wavelength. Inflection points occurring outside the tested range of concentrations are not shown here. The black dashed line represents the inflection points of particle size correlation shown in Figure 6 above.

A series of representative bands were selected for analysis in Figure 6. For the selected wavelength bands, the hyperspectral spectra show different behaviors depending on sediment sizes and concentration. From the aspect of particle sizes, two regions can be identified depending on the correlation between radiance and particle sizes, which can be defined as positive and negative correlation regions. For the wavelength of 452 nm, only a positive correlation region is present, while with higher wavelengths, the negative correlation region extends from low concentration to high concentration. At the highest wavelength of 954 nm, only a negative correlation region is present. This observation can be used to design algorithms to determine particle sizes using water color.

In terms of the variation of concentration, the data can also be divided into positive and negative correlations, with the peaks marking the inflection points, i.e. the radiance increases and then decreases with the concentration. The smaller the particle size the lower concentration the peak appears. In addition, the peak shifts to higher concentrations in higher wavelengths. This provides a complicated pattern of the concentration dependence and one who develops a remote sensing method to determine particle concentration should be careful about the water color which may indicate different concentrations and thus must be limited to a range of concentrations for monotonic relationship for reliable determination.

Figure 7 shows the inflection points or maximums for each wavelength and size. For the concentrations associated with each point, lower concentrations have a positive correlation with radiance. We note that the bands 400-430 nm have noise – ignoring these bands shows a general trend of greater wavelength bands having higher inflection points for larger concentrations. As seen in Figure 6, the larger wavelengths do not have inflection points within the range of concentrations that were tested. This is also true for smaller sizes at low wavelengths: no inflection points are shown in Figure 7 for these cases. The inflection points about particle size correlation are also labeled in Figure 7. The trend of the line is similar to the concentration correlation, but the region of correlation is opposite to the concentration – the right of the line is a region of positive correlation and the left of the line marks negative correlation.

To estimate the differences among varying particle sizes and concentrations, we define the hyperspectrum of each case as a vector, ranging from the lowest wavelength (400 nm) to the highest (1000 nm). The vector for the white background control serves as a reference, and the L2-norm for each case relative to this reference is calculated, as shown in Table 2. The results in Table 2 indicate that higher concentrations generally correspond to greater difference from the control, and this is more obvious for large particles than small. At low concentrations (<2 mg/L), the cases with a particle diameter of 75-150 μm are closest to the white control, whereas, at relatively high concentrations, the lowest difference shifts to a particle diameter of 30-75 μm.

By taking the gradient of the values in Table 2 with respect to concentration, we determined the sensitivity of hyperspectral imaging to concentration variations in Table 3. The table indicates that low concentrations generally result in higher sensitivity to concentration changes, and smaller particles exhibit greater sensitivity than larger particles.

Table 4 presents the gradient of the hyperspectral vectors with respect to particle sizes. In general, smaller particles exhibit more sensitivity to changes in particle size, while both low and high concentrations show higher sensitivity to particle size changes compared to moderate concentrations. This surprising result might be due to the fact that moderate concentrations have a flatter hyperspectrum, as shown in Figure 6.

Table 5 lists the most sensitive band for each case. Typically, higher concentrations and smaller particles are more sensitive at higher wavelengths, with the most sensitive bands concentrated in the red and near-infrared (NIR) regions. It is also important to note that the extreme high and low ends of the spectrum are noisier, which means that the spectra for low concentrations and large particles exhibit some noise and do not follow the general trend.

Table 2. L2 norm of the difference (mW $*m^{-2}*sr^{-1}$) of each case from the vector of white control

Diameter (μm)	Concentration (mg/L)								
	0.1	0.2	0.4	0.6	0.8	1	2	4	10
0-75	0.722	1.085	1.372	1.460	1.495	1.472	1.530	1.694	1.922
30-75	0.238	0.718	0.990	1.111	1.146	1.146	1.139	1.160	1.305
75-150	0.066	0.186	0.413	0.556	0.696	0.710	1.139	1.646	1.902
150-250	0.251	0.308	0.462	0.616	0.756	0.769	1.253	1.818	2.407

Table 3. Gradient ($mW*m^{-2}*sr^{-1}*mg^{-1}*L$) of the vector difference regarding the concentration.

	Concentration (mg/L)							
Diameter (μm)	0.2	0.4	0.6	0.8	1	2	4	10
0-75	3.626	1.435	0.439	0.176	0.117	0.058	0.082	0.101
30-75	4.799	1.357	0.605	0.176	0.001	0.007	0.011	0.024
75-150	1.201	1.134	0.717	0.698	0.071	0.429	0.182	0.030
150-250	0.568	0.771	0.771	0.700	0.062	0.484	0.262	0.602

Table 4. Gradient (x0.01 mW* $m^{-2}*sr^{-1}$ μm^{-1}) of the vector difference regarding the particle diameter.

Diameter (μm)	Concentration (mg/L)								
	0.1	0.2	0.4	0.6	0.8	1	2	4	10
30-75	3.227	2.445	2.548	2.327	2.327	2.169	2.603	3.557	4.114
75-150	0.288	0.888	0.962	0.924	0.751	0.728	0.001	0.809	0.996
150-250	0.212	0.140	0.056	0.069	0.069	0.067	0.130	0.197	0.577

Table 5. The most sensitive band in each case.

Diameter (μm)	Concentration (mg/L)								
	0.1	0.2	0.4	0.6	0.8	1	2	4	10
0-75	679	679	684	690	690	841	841	884	927
30-75	668	679	679	684	684	684	841	884	927
75-150	414	663	668	673	679	679	679	684	841
150-250	997	986	986	679	679	679	679	684	841

4. Discussion

Based on the analysis, the most effective bands for detecting variations in concentration and particle size are situated in the red and near-infrared (NIR) regions of the spectrum, which is consistent with the earlier study of [10]. Higher concentrations and smaller particles demonstrate increased sensitivity at these higher wavelengths. This information can be leveraged to design more targeted hyperspectral imaging systems or other remote sensing technology for suspended sediments. By focusing on these specific bands, one can enhance the detection capabilities and accuracy for both concentration and particle size measurements. Emphasizing red and NIR bands could significantly improve the precision in identifying finer distinctions in sediment characteristics, thereby optimizing data collection and analysis processes in future experiments.

The diagram of the inflection points is the first time to reveal the complicated physics in the light scattering of the suspended sediment solution. It highlights the necessity to carefully design the remote sensing scheme to determine the concentration and particle sizes of suspended sediment. Specifically, our study showed that for the same radiance strength, there exist multiple concentration or particle sizes. A linear or monotonic correlation is limited to the application in the field. To design a more reliable determination scheme, researchers must consider the radiance in different wavelengths and their trends to formulate the correct strategy for measurements.

Despite the promising results, there are inherent uncertainties in the data. A notable source of uncertainty arises from the noise present at the extreme high and low ends of the spectrum. This noise particularly affects the spectra of samples with low concentration and large particles, leading to deviations from the expected trends. Such uncertainties need to be accounted for in the interpretation of hyperspectral data to ensure robustness in the conclusions drawn.

The experimental setup is not without its limitations. For instance, the use of a single white background control may not adequately account for variations in background interference in different real-world scenarios. Additionally, the particle sizes and concentrations studied are limited in range, potentially overlooking important variations outside this range. The experimental environment should ideally mimic field conditions more closely to provide more generalizable results. Other limitations include potential inconsistencies in particle distribution and the stability of the hyperspectral imaging device itself.

The data analysis process also has its share of uncertainties. The method of calculating the L2-norm and gradients is sensitive to variations in initial conditions and noise. The assumptions made during the data normalization and preprocessing stages could introduce biases that might affect the final results. Moreover, the linear approach to gradient calculation might oversimplify the complex interactions between particle size, concentration, and hyperspectral response. A more robust statistical analysis or machine learning techniques may be employed to improve the reliability of findings.

To build upon this study, future research should consider field studies to validate the laboratory findings under real-world conditions. Different types of sediments with a broader range of particle sizes and concentrations should be investigated to enhance the generalizability of the results. Improved experimental setups that mitigate current limitations and incorporate advanced data processing techniques would also be beneficial. Additionally, exploring the effectiveness of hyperspectral imaging across various environmental settings and sediment types could provide deeper insights and contribute significantly to the fields of environmental monitoring and remote sensing.

5. Conclusions

In this study, we investigated the hyperspectral imaging response to varying particle sizes and concentrations in sediment samples. By defining hyperspectral vectors and calculating their L2-norms relative to a white background control, we were able to discern patterns and sensitivities among different particle size and concentration scenarios. Our findings indicate that higher concentrations generally correspond to higher L2-norm values, and the sensitivity of hyperspectral imaging to concentration changes is most pronounced at lower concentrations and for smaller particles.

Furthermore, the analysis revealed that the red and near-infrared (NIR) bands are particularly effective in detecting variations in concentration and particle size, suggesting that future hyperspectral imaging systems should focus on these regions to achieve greater sensitivity and accuracy. We also identified noise at the extreme ends of the spectrum, which introduces some uncertainty into the data, particularly for low concentrations and large particles.

This study is probably the first time to reveal the complicated scattering physics associated with suspended sediment solution. First, the correlation of the radiance with concentration and particle size was found opposite for the low and high levels of concentration. Second, inflection points of the correlations have the same trend to increase with higher wavelengths. Third, the sensitivity of the radiance is complicated: the radiance is more sensitive to concentration variance in low concentration and more sensitive to particle size for smaller particles.

Our study is not without limitations, including the potential variability introduced by using a single white background control and the constrained range of particle sizes and concentrations examined. These limitations, along with the inherent uncertainties in data analysis methods, highlight the need for further research to confirm and extend our findings.

In conclusion, our results underscore the potential of hyperspectral imaging as a powerful tool for analyzing sediment characteristics, particularly when leveraging the higher sensitivity of the red and NIR bands. Future research should aim to validate these findings in real-world field studies and across a wider variety of sediment types. Additionally, refining experimental setups and data analysis techniques will be crucial in advancing the application of hyperspectral imaging in environmental monitoring and remote sensing.

Author Contributions: David Bazzett: Conceptualization, Visualization, Methodology, Resources, Data curation, Formal analysis, Investigation, Software, Writing - original draft. **Roger Wang:** Conceptualization, Visualization, Resources, Supervision, Validation, Writing - review & editing, Project administration.

Funding: This research received no external funding.

Data Availability Statement: Code and data are available on github and figshare below:
https://github.com/david-b-project/hyperspectral-sediment
https://figshare.com/articles/dataset/Hyperspectral_data/26000143

Acknowledgments: The authors would like to acknowledge the contributions from the following students: Akanksha Ramabadran, Srinidhi Ayalasomayajula, Vijay Chandhar Marimuthu Anur, Catherine McDonnell, Dawid Zieba, and Hamza El-Hawwat.

Conflicts of Interest: The authors declare no conflicts of interest.

References

1. U.S. Environmental Protection Agency (EPA), Method 180.1 Determination Of Turbidity By Nephelometry, **1993**
2. Pinet, S., Martinez, J.-M., Ouillon, S., Lartiges, B., Villar, R.E., Variability of apparent and inherent optical properties of sediment-laden waters in large river basins – lessons from in situ measurements and bio-optical modeling. *Opt. Express*, 2017, https://doi.org/10.1364/oe.25.00a283
3. Kwon, S., Noh, H., Seo, I.W, Park, Y.S, Effects of spectral variability due to sediment and bottom characteristics on remote sensing for suspended sediment in shallow rivers. *Science of the Total Environment*, **2023** https://doi.org/10.1016/j.scitotenv.2023.163125
4. Kitchener, B.G.B., Wainwright, J. and Parsons, A.J. A review of the principles of turbidity measurement. *Progress in Physical Geography*, **2017,** *41 (5).* pp. 620-642., ISSN 0309-1333, https://doi.org/10.1177/0309133317726540
5. Tassan, S., Local algorithms using SeaWiFS data for the retrieval of phytoplankton, pigments, suspended sediment, and yellow substance in coastal waters. *Appl. Opt*., **1994,** *33 (12)*, 2369–2378., https://doi.org/10.1364/AO.33.002369.
6. Binding, C.E., Bowers, D.G., Mitchelson-Jacob, E.G., Estimating suspended sediment concentrations from ocean colour measurements in moderately turbid waters; The impact of variable particle scattering properties. *Remote Sens. Environ*. **2005**, *94*, 373–383., https://doi.org/10.1016/j.rse.2004.11.002.
7. Long, C.M., Pavelsky, T.M., Remote sensing of suspended sediment concentration and hydrologic connectivity in a complex wetland environment. *Remote Sens. Environ*., **2013**, *129*, 197–209., https://doi.org/10.1016/j.rse.2012.10.019.
8. Ritchie, J.C., Schiebe, F.R., McHenry, J.R.,. Remote sensing of suspended sediments in surface waters. *Photogramm. Eng. Remote Sens.*, **1976,** *42 (12),* 1539–1545.
9. Li, J., Tian, L., Song, Q., Haung, J., Li, W., Wei, A., A Near-Infrared Band-Based Algorithm for Suspended Sediment Estimation for Turbid Waters Using the Experimental Tiangong 2 Moderate Resolution Wide-Wavelength Imager, *IEEE J. Of Selected Topics In Applied Earth Obs. And Remote Sensing*, **2019**, DOI: 10.1109/JSTARS.2019.2896729
10. Kwon, S., Shin, J., Seo, I.W., Noh, H., Jung, S.H., You, H.,. Measurement of suspended sediment concentration in open channel flows based on hyperspectral imagery from UAVs. *Adv. Water Resour*., **2022**, 159, 104076. https://doi.org/10.1016/j.advwatres.2021.104076.
11. Yepez, S., Laraque, A., Martinez, J.M., De Sa, J., Carrera, J.M., Castellanos, B., Gallay, M., Lopez, J.L., Retrieval of suspended sediment concentrations using Landsat-8 OLI satellite images in the Orinoco River (Venezuela). *Comptes Rendus - Geosci*. **2018**, *350*, 20–30. https://doi.org/10.1016/j.crte.2017.08.004
12. Prior, E., O'Donnell, F., Brodeck, C., Runion, G.B., Shepherd, S.L., Investigating small unoccupied aerial systems (sUAS) multispectral imagery for total suspended solids and turbidity monitoring in small streams, *Int'l J. of Remote Sensing,* **2021,** , *42,* p39-46, https://doi.org/10.1080/01431161.2020.1798546
13. Landgrebe, D. Information extraction principles and methods for multispectral and hyperspectral image data. *Inf. Process. Remote Sens.* **1999**, 82, 3–38
14. Khan, M. J., Khan, H. S., Yousaf, A., Khurshid, K., and Abbas, A. Modern Trends in Hyperspectral Image Analysis: a Review. *IEEE Access 6*, **2018,** *14118–14129*. doi:10.1109/access.2018.2812999
15. Lu, B., Dao, P., Liu, J., He, Y., Shang, J, Recent Advances of Hyperspectral Imaging Technology and Applications in Agriculture *Remote Sens*. **2020**, 12, 2659; doi:10.3390/rs12162659